Combining Structural and Electrochemical Analysis of Electrodes Using Micro-Computed Tomography and a Microfluidic Fuel Cell

Journal of The Electrochemical Society, **159** (3) B292-B298 (2012)
0013-4651/2012/159(3)/B292/7/$28.00 © The Electrochemical Society

Combining Structural and Electrochemical Analysis of Electrodes Using Micro-Computed Tomography and a Microfluidic Fuel Cell

Huei-Ru (Molly) Jhong,[a,*] Fikile R. Brushett,[a,*] Leilei Yin,[b] Darren M. Stevenson,[b] and Paul J. A. Kenis[a,b,,z]**

[a]*Department of Chemical & Biomolecular Engineering and* [b]*Beckman Institute, University of Illinois at Urbana-Champaign, Urbana, Illinois 61801, USA*

Detailed investigation of the relationship between the physical structure and electrochemical activity of state-of-the-art fuel cell electrodes is a critical, yet often poorly reported or proprietary, step in the manufacturing of cheaper and more durable configurations. Here we demonstrate the utility of X-ray micro-computed tomography (MicroCT) for detailed characterization of the architecture and buried interfaces of fuel cell electrodes in a non-destructive fashion. We employ a combined thresholding and filament tracing based analytical protocol for image analysis which enables more accurate quantification of GDE structures as compared to previously-used thresholding-only methods. Furthermore, we report on a methodology of combining in-situ electrochemical analysis in a microfluidic fuel cell and *ex-situ* structural analysis in a MicroCT which enables direct correlation of changes in electrode performance to changes in physical structure, in this case, porosity. As a demonstration, the effects of electrode compression are investigated. We observed that both subtle shifts in structure in the microporous and catalyst layers at low compression pressures ($<1 \times 10^3$ lb_f) and more drastic structural densification of the macroporous carbon fiber layer at moderate compression pressures ($\geq 1 \times 10^3$ lb_f) impact electrode performance.
 [DOI: 10.1149/2.033203jes]

Manuscript submitted September 19, 2011; revised manuscript received November 28, 2011. Published January 3, 2012.

Low temperature fuel cells, such as polymer electrolyte membrane fuel cells (PEMFCs), have been extensively investigated as alternative power sources due to their high efficiency, high energy density and low emissions.[1,2] Unfortunately, commercialization of these technologies has been hampered by high cost and insufficient durability.[3] Reducing cost and improving durability of these fuel cell systems requires detailed studies of each component (e.g., electrodes, membranes, flow-fields) and of the interfaces between those components (e.g., membrane-electrode). Of particular importance are gas diffusion electrodes (GDEs), which consist of a catalyst layer, a microporous layer (MPL) of teflonized carbons, and a macroporous layer of carbon fibers.[4] The GDE structure plays a pivotal role in fuel cell operation as it functions (*i*) to deliver reactant gas from flow-field channels to catalyst layer, (*ii*) to drain liquid water from the catalyst layer into flow channels or the electrolyte/membrane, and (*iii*) to conduct electrons with low resistance.[4] Maximizing electrode performance, and consequently fuel cell performance, requires optimizing all of these transport processes that strongly depend on the complex three-dimensional (3D) structure of the GDE. Unfortunately, these structure-activity relationships remain poorly-understood as (*i*) present state-of-the-art electrodes are often manufactured using proprietary methods and (*ii*) physical changes in electrode structure, both macro and micro, during fuel cell operation have not been extensively studied. The rational design of novel high-performance electrodes requires a detailed understanding of how GDE structure and performance change as a function of preparation methods and operational conditions. Therefore, a systematic characterization of electrode structure and subsequent performance as a function of processing parameters, including electrode compression during pretreatment, catalyst deposition, and membrane-electrode assembling, is needed. However, in the absence of non-destructive 3D imaging techniques, gaining a comprehensive understanding of GDE structure-activity relationships is difficult.

Traditional methods for analyzing electrode structure such as scanning electron microscopy (SEM) probe two-dimensional (2D) surfaces/cross-sections and thus provide limited information on how buried interfaces are interconnected in 3D. SEM imaging coupled with ion milling (i.e., focused ion-beam-scanning electron microscopy, FIB-SEM) can be used to generate 3D microstructural renderings, albeit in a destructive fashion. This technique has been applied successfully to solid-oxide fuel cell (SOFC) anodes[5] as well as the catalyst layer and the MPL of PEMFCs.[6,7] Unfortunately, FIB-SEM is not suitable for studying *dynamic* GDE structure-activity relationships due to (*i*) destructive sample preparation, (*ii*) limited field of view, 10 μm $\times$ 10 μm at most, in comparison to typical GDE thicknesses of 200–500 μm, and (*iii*) computational costs (i.e., more time needed to analyze a dataset with nanoscale pixels). X-ray tomography is an emerging analytical technique in fuel cell science that enables non-destructive multiscale 3D imaging of electrode architecture and liquid water transport through that architecture.[6,8–20] In X-ray tomography, an X-ray beam travels through a rotating sample and its intensity gets attenuated. The transmitted signals are then collected by a detector to generate a 3D map of variations in X-ray absorption within the sample, from which different phases/elements as well as heterogeneity in density can be identified.[8] Two X-ray tomography methods are available: X-ray micro-computed tomography (MicroCT) and X-ray nano-computed tomography (NanoCT) provide resolutions of 1–10 μm and $\leq$100 nm, respectively.[17] While NanoCT has been employed to analyze electrode structure, particularly to analyze features at the sub-micron length scale, its utility is limited to evaluating sub-millimeter size samples.[6,17,21] Furthermore, NanoCT is also more computationally expensive than MicroCT. To date, most MicroCT investigations of fuel cells have focused on the study of water management in PEMFC cathodes[10,11,13] and, more recently, the structural analysis of electrode architectures with a focus on providing more accurate parameters for numerical models.[15,18,20] To our knowledge, to date no efforts have focused on the systematic investigation of structure-activity relationships as a function of electrode preparation methods, in which individual electrode performance is directly linked with electrode structure.

Here, we report an analytical methodology that directly correlates changes in electrode performance, as measured *in-situ* using a microfluidic H_2/O_2 fuel cell, to changes in physical structure (i.e., porosity), as determined *ex-situ* using MicroCT. In specific, we demonstrate the utility of MicroCT to characterize buried interfaces of fuel cell electrodes in detail in a non-destructive fashion.

Experimental

GDE preparation and fuel cell testing.— EFCG Phosphoric Acid Fuel Cell Electrodes (E-Tek) were used as gas diffusion layers (GDLs) in this study. This GDL consists of a polytetrafluoroethylene (PTFE)-

* Electrochemical Society Student Member.
** Electrochemical Society Active Member.
z E-mail: kenis@illinois.edu

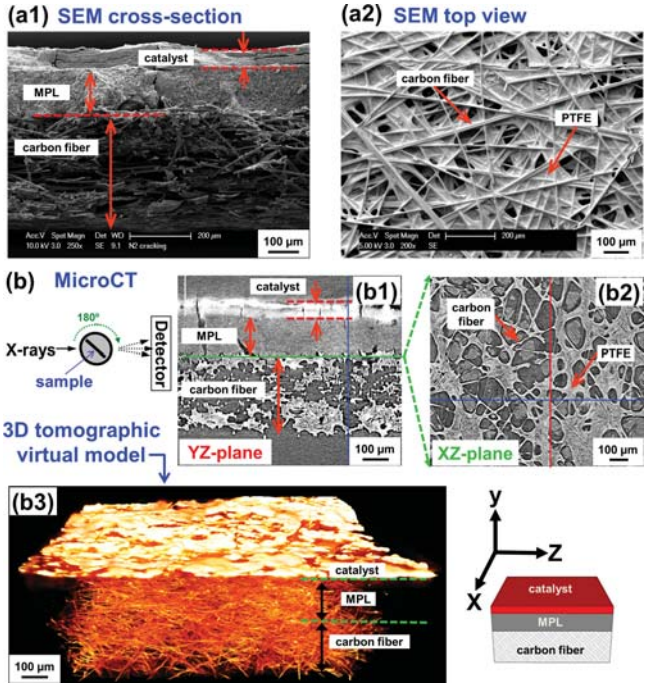

Figure 1. Cross-sectional view (a1) and top view (a2) SEM micrographs of a gas diffusion electrode (GDE) with an air-brushed Pt/C catalyst layer. (b) Setup for MicroCT imaging of a GDE with an air-brushed Pt/C catalyst layer, resulting in an initial reconstruction of the MicroCT data to generate 2D radiographic cross-sectional images in the YZ-plane (b1, through-plane), XZ-plane (b2, in-plane), and XY-plane (also through-plane, not shown) as well as a 3D tomographic virtual model (b3). The colored lines in the 2D images represent the corresponding YZ-plane (red line), XZ-plane (green line), and XY-plane (blue line).

treated Toray carbon paper TGP-H-120 with a teflonized microporous layer on one side. Catalyst inks were prepared by mixing 12 mg Pt/C catalyst (50 wt% Pt) and 9.2 µL Nafion solution (5 wt%, Solution Technology, 30:1 catalyst-to-Nafion ratio), and adding the carrier solvents: 200 µL of Millipore water (18.2 MΩ), and 200 µL of isopropyl alcohol. All catalyst inks were sonicated (Branson 3510) for at least two hours to ensure uniform mixing and were hand-painted on the teflonized carbon side of the GDL to create a gas diffusion electrode (GDE) covered with catalyst over a geometric surface area of 4 cm^2. So the catalyst loading is 3 mg Pt/C/cm^2. Some of the fabricated GDEs were hot-pressed (Carver 3851-0) at varying pressures (0, 1×10^3, 2×10^3, 5×10^3 and 10×10^3 lb_f) and at a temperature of $125 \pm 10^{\circ}C$ for 5 min. Detailed descriptions of fuel cell assembly and testing procedures can be found in our previous work.[22,23]

Acquisition, reconstruction, and segmentation of MicroCT data.— In this study, the whole GDE was clamped in a rotating sample holder and a corner was exposed to the X-ray beam field (Figure 1b, top left). During MicroCT imaging (Micro-XCT 400, Xradia), the sample was scanned using an X-ray source at 40 kV and 200 µA, and 745 projections, typically called shadowgraphs or shadow images, were collected as the sample was rotated stepwise over 180° with a 10 second exposure time for each projection. The shadow images were then processed to reconstruct 2D radiographic cross-sectional image stacks and 3D tomographic virtual models of the GDE. The initial reconstruction of MicroCT data was carried out using the *TXM Reconstructor* reconstruction software (Xradia), which accompanies the MicroCT hardware. The distances of the sample to the X-ray source (76 mm) and the X-ray detector (28 mm) resulted in a voxel (volume pixel) size of 1 μm^3. The field of view (FOV) was approximately 1000 µm × 1000 µm. Further image processing was performed using the *Amira* visualization software package (Version 5.3, Visage Imaging) for subsequent quantitative analysis of the GDE microstructure.

Results and Discussion

Qualitative visualization of GDE structure.— Figure 1 shows comparative GDE imaging by SEM and MicroCT. Obtaining cross-sectional images of a GDE using a SEM without physically slicing off the material is difficult. Breaking the GDE via liquid nitrogen cracking (Figure 1a1) or cutting thin slices off of the GDE using a razor blade tends to cause damage to or smearing of the porous structure.[7] Figure 1a2 shows the 2D SEM micrograph of a GDL in a bottom up view which provides only information on the surface of the macroporous backing layer. In contrast, MicroCT as a non-destructive imaging technique does not require destructive sample preparation to generate cross-sectional images. The initial data reconstruction obtained with MicroCT allows for inspection of 2D radiographic cross-sectional image stacks and of 3D tomographic virtual models of the GDE, which provides detailed information about layer thickness, internal architecture, and material distribution. In particular, Figure 1b1 b2 shows through-plane (YZ-plane) and in-plane (XZ-plane) 2D radiographic images of the GDE, respectively. In these images, one can easily distinguish the catalyst layer, the microporous layer, and the macroporous carbon fiber layer by comparative layer thicknesses as well as brightnesses (Figure 1b1), and within the layers one can distinguish the distribution of different materials, e.g., carbon fibers vs. PTFE (Figure 1b2). We confirm that the bright catalyst layer in Figure 1b1 is not an artifact of beam hardening. In addition to layer thickness provided by through-plane images, buried layer interfaces can also be characterized from examination of in-plane images. For example, Figure 1b2 shows the interface between the macroporous backing layer comprised of fibrous carbons and the hydrophobic MPL comprised of a polytetrafluoroethylene (PTFE) and carbon particle mixture. In addition, the 3D tomographic virtual model of the GDE (Figure 1b3) visualizes the internal architecture and organization in false color. The brightness of the false color indicates X-ray absorption intensity of materials, so materials with high atomic numbers or densities such as metallic catalyst particles tend to be brighter. While the microporous layer and the macroporous layer are both carbonaceous, the macroporous, fibrous layer tends to be much brighter due to its higher carbon density whereas the microporous layer that consists of low-density teflonized carbon particles appears relatively invisible. In sum, MicroCT imaging provides information on *(i)* buried interfaces, *(ii)* 3D architecture, and *(iii)* material distribution, which is critical in understanding transport processes within the electrode.

Methodology for quantitative analysis of GDE structure.— Computing microstructural properties of GDEs, such as porosity and pore size distribution, from MicroCT data has gained a lot of interest to validate numerical models of electrode material properties.[15,20,24] Here, we quantify these structural properties to understand the extent to which physical changes in electrode structure correlate to changes in electrode performance. We have developed an analytical methodology to post-process the 2D radiographic cross-sectional images obtained from the initial reconstruction to extract critical structural parameters from the MicroCT data, including information of the bulk porosity of and local porosity within the macroporous layer.

Figure 2a shows the flowchart of this quantitative analysis procedure. First, the 2D cross-sectional image stack is cropped to a discrete volume that is of analytical interest, here a 862 µm × 658 µm × 345 µm section of the macroporous layer. The analytical volume is selected based on two criteria: *(i)* the analytical volume is the majority of the total image volume of the macroporous layer (i.e., 862 µm × 685 µm × 400 µm), and *(ii)* the analytical volume does not include or is not close to either the macroporous layer – air interface or the macroporous layer – MPL interface. Sensitivity analysis is performed on 10 samples of the same GDL material to determine if this volume is representative of the material properties and similar results are obtained, for example, the bulk porosity is $70.6 \pm 0.9\%$.

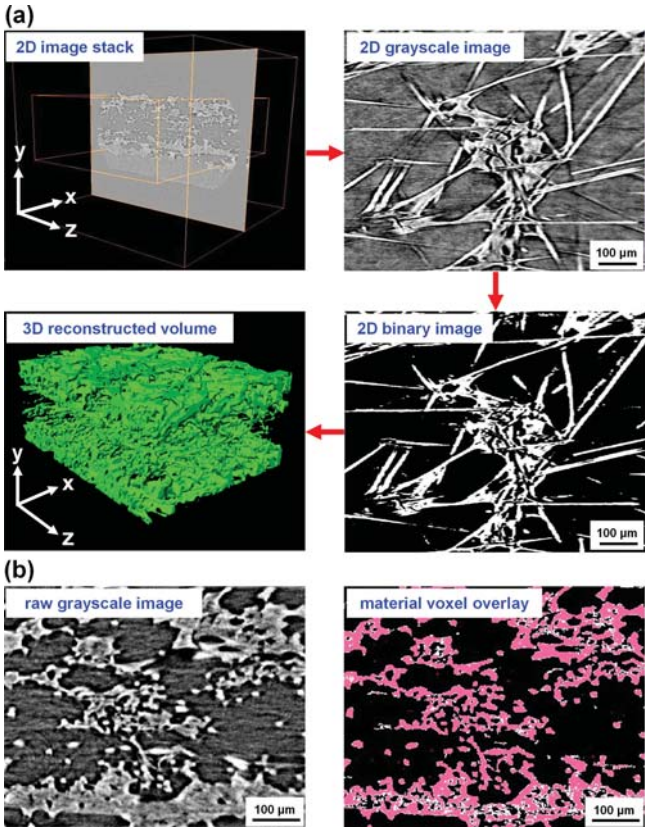

Figure 2. (a) A flow-chart of the quantitative analysis procedure used to characterize GDE microstructure. Here, a volume section of 862 µm × 658 µm × 345 µm (x × y × z) of the macroporous layer is analyzed. From the 2D image stack, each 2D grayscale image is segmented to result in a 2D binary image, which in turn helps to identify and separate voxels as predominantly filled with material (white) from those predominantly void (black). Next a 3D volume is reconstructed from the binary images, showing carbon fibers (green, false color) and void space (black), for subsequent quantitative analysis. (b) A side-by-side comparison of the raw grayscale image (left) and material voxel overlay of the binary images generated with each of the two segmentation methods (right): in red and white material voxels identified using the thresholding and the filament tracing method, respectively. Material voxels identified by both methods are pink.

Second, each 2D grayscale image is segmented to a 2D binary image to help identify and separate voxels predominantly filled with materials (white) from those that are predominantly void (black). Two segmentation techniques are investigated: the *thresholding method* and the *filament tracing method*. In the most commonly used segmentation method, image thresholding, the threshold value of the grayscale range is determined either by visual inspection or by an algorithm (i.e., Otsu's method) that attempts to simultaneously account for all of material without capturing excessive void space.[17,20,25] However, this thresholding method does not accurately filter out image noise, e.g., due to the effects of X-ray beam hardening. Consequently, grayscale values can be found in the fibrous masses and also in the void space, especially close to the edges of the fibers (Figure 2b). Figure 2b shows the raw grayscale image as well as an overlay of the binary images generated by each of the two segmentation methods. The overlaid binary images highlight the differences between the material voxels identified using the thresholding method (red) and the filament tracing method (white). The pink and black areas represent method overlap and void space, respectively.

In this study, we perform segmentation using the *filament tracing method*, available in Amira v5.3 visualization software, which utilizes a grayscale threshold value in combination with structural connectivity, rather than a threshold range alone.[26] As a result, this method better differentiates fibrous masses from void space. Connected carbon fibers are identified in a single slice using a semi-automated operation, comprised of threshold masking followed by edge detection. Specifically, threshold masking permits the user to first select a grayscale *range* (by visual inspection) prior to employing further segmentation algorithms. The grayscale threshold (a range) is determined by subjective visual inspection that is considered more effective than automated methods when distinctive and easily computer-recognizable boundaries are not present,[27,28] which is the case here in the analysis of GDEs. The threshold masking limits which grayscale values can or cannot be selected, effectively creating a new sub-volume of available intensity values for segmentation. This type of masking is especially helpful when applying subsequent algorithms such as edge detection, which rely upon the computational ability to automatically distinguish between structural components in an image. The edge detection we used relies upon the three-dimensional region growing algorithm,[26] which starts from a user-defined seed point and segments images by incrementally recruiting voxels based on predefined criteria, including grayscale value similarity and spatial proximity. The voxels that are connected and have similar grayscale values are assumed belonging to the same material. These connected fibers that are identified in a single slice are then automatically traced throughout the entire analytical volume such that only connected volumes, within the threshold grayscale range, are captured.

After segmentation, in the third and final step, a 3D reconstructed volume of these binary images is rendered for subsequent quantitative analysis. For example, the properties of the macroporous layer can be investigated with a focus on determining both bulk porosity and layer-to-layer changes in porosity. The porosity ε is defined as: $\varepsilon = 1 - (\text{material}_{vox})/(\text{material}_{vox} + \text{void}_{vox})$, where material_{vox} is the number of material voxels filled with carbon fibers, binder, or PTFE (all of which are assumed to be impermeable) and void_{vox} is the number of void voxels.

With the porosity data obtained directly from MicroCT, critical physical properties such as tortuosity, relative diffusivity, and permeability that govern the delivery of reactant gases and removal of products within the GDL can be calculated using equations proposed by numerical models such as the Bruggeman model[29] as well as the Tomadakis & Sotirchos model.[30,31] Accurate knowledge of these transport properties is needed to improve the power density and efficiency of PEMFCs. Moreover, these parameters are necessary input for all numerical models simulating multi-phase mass transport within the GDL.[15]

In PEMFCs, the mass transport of reactant gases from the flow channels to the catalyst layer is dominated by diffusion.[32] Binary diffusion of species a and b in a porous medium can be described by Fick's first law and effective media theory:

$$j = -D_{ab}^{eff} \nabla c, \qquad [1]$$

where c is the concentration, and j is the molar flux. D_{ab}^{eff} is the effective diffusion coefficient tensor, which is split into an effective relative diffusivity $f(\varepsilon)$ and a bulk diffusivity D_{ab}:

$$D_{ab}^{eff} = f(\varepsilon) D_{ab} = \frac{\varepsilon}{\tau} D_{ab}, \qquad [2]$$

where ε is the porosity and τ is the tortuosity, a measure for the connectivity of the pores. Mathematically the tortuosity is defined as the arc-to-chord ratio, which is the ratio of the length of a curve to the distance between the end points.[33] Typically, the Bruggeman model (Eq. 3),[29] which is based on an idealized morphology of *spherical* agglomerates, is used for tortuosity and effective relative diffusivity prediction due to its simplicity. However, application of this model to *fibrous* agglomerates is known to be not very accurate.[24,33] Tomadakis & Sotirchos[30,31] developed a model for randomly oriented fibrous media. This model uses Monte Carlo simulation on constructed fibrous media to compute tortuosity and effective relative diffusivity as a function of porosity and proposes the following equations with porosity

as the only input parameter:

$$\tau = \left(\frac{1-\varepsilon_p}{\varepsilon-\varepsilon_p}\right)^{\alpha} \text{ and} \quad [3]$$

$$f(\varepsilon) = \varepsilon\left(\frac{\varepsilon-\varepsilon_p}{1-\varepsilon_p}\right)^{\alpha}, \quad [4]$$

where ε_p is the percolation threshold porosity, the porosity with the least required open void space connectivity for diffusion or permeation through the porous media (here $\varepsilon_p = 0.11$), and α is a fitting parameter for through-plane diffusion (here $\alpha = 0.785$). ε_p was determined by extrapolating the simulation results of effective relative diffusivity to the minimum porosity that allows mass transfer to occur. α was determined using a parameter estimation procedure based on the minimization of the square error between the simulations and the proposed equations.

Although diffusion is considered the primary mode of gas-phase transport within the GDE, convection needs to be accounted for when a pressure difference exists between neighboring flow channels.[32,34] Convection in a porous medium can be described by Darcy's law:

$$u = -\frac{\kappa}{\mu}\nabla P, \quad [5]$$

where κ is the permeability tensor, μ the dynamic viscosity of the fluid, u the velocity of the fluid, and P is the pressure. Tomadakis & Sotirchos[30,31] predicts the permeability using:

$$K = \frac{\varepsilon}{8(\ln\varepsilon)^2}\frac{(\varepsilon-\varepsilon_p)^{(\alpha+2)}r_f^2}{(1-\varepsilon_p)^{\alpha}[(\alpha+1)\varepsilon-\varepsilon_p]^2} \quad [6]$$

where r_f is the carbon fiber radius. We use $r_f = 4.6\ \mu$m, which is in agreement with values reported in literature[34] as well as our observations in SEM. The applicability of the Tomadakis & Sotirchos model to GDLs has been validated by experimental data and observations.[34]

Recently, Fishman et al.[24] employed the Tomadakis & Sotirchos model to calculate heterogeneous through-plane distributions of tortuosity, relative permeability, and permeability for GDLs. These analyses provided insight into the impact of GDL porosity on transport properties. Here, we exploited a similar analysis for the calculation of transport properties using porosity data we obtained from MicroCT using the filament tracing segmentation procedure described above (Figure 2a). Specifically, we wished to get a better understanding on how these transport properties respond to electrode preparation methods, for example, the mechanical compression of the GDE. Due to the non-destructive nature of MicroCT imaging, the exact same GDE can be investigated multiple times after being exposed to and tested at different conditions for different periods of time. For example, we studied the relation between changes in electrochemical performance and changes in electrode structure by sequentially exposing the same electrode to higher compression levels. This MicroCT-based method allows for porosities to be measured and, from that, for the determination of the corresponding physical properties of tortuosity, relative diffusivity, and permeability, without the need to perform destructive measurements like mercury intrusion porosimetry (MIP).

An example study of linking electrode structure and performance.— Combined *ex-situ* MicroCT imaging and *in-situ* fuel cell analysis can be used to systematically probe the impact of physical changes in the electrode structure on its electrochemical performance. Furthermore, the use of a microfluidic fuel cell enables structure-activity relationships to be determined for individual electrodes within an operating fuel cell. To demonstrate the utility of such investigations, we studied the effects of hot-pressing on fuel cell electrode performance. Prior to use, fuel cell electrodes and membrane-electrode assemblies (MEAs) are hot-pressed to compact the interfacing layers together in order to minimize electrical contact resistances and to avoid delamination. In addition, pressure is also applied to the fuel cell stack during operation to prevent gas leaks and to ensure minimal contact resistance losses between electrodes or MEAs and current collectors. However, over-compression of or uneven pressure distribution across GDEs can damage the intricate electrode microstructure leading to losses in porosity and consequently to a reduction in performance and durability. Thus, understanding and balancing these competing effects is important for the design and development of next-generation electrode materials and fuel cell systems. Despite its importance, to date relatively few papers have been published on the effects of mechanical compression on electrode performance. Lee et al.[35] studied the effect of GDL compression on PEMFC performance by adjusting the bolt torque for different GDL materials and found optimal bolt torque values. Ge et al.[36] found that the amount of compression has a significant impact on PEMFC performance and the optimal compression varies for different GDL materials. Bazylak et al.[37] studied the influence of GDL compression on the morphology of the GDL using SEM and suggested the irreversible damage to carbon fibers as well as PTFE in the macroporous layer results in preferential pathways for excess water transport, which leads to electrode flooding. So in prior work, either electrochemical analysis or structural analysis has been reported. Here, we will study the effects of compression on both GDE structure and electrochemical activity.

Figure 3 and 4 show combined electrochemical and structural analysis of the effects of hot-pressing on acidic fuel cell cathode performance. Cathode performance typically limits the overall acidic fuel cell performance due to sluggish oxygen reduction reaction (ORR) kinetics and insufficient removal of water generated by the ORR, which leads to flooding. Thus cathode performance is dependent on the ability of the electrode to efficiently deliver oxygen to the catalyst

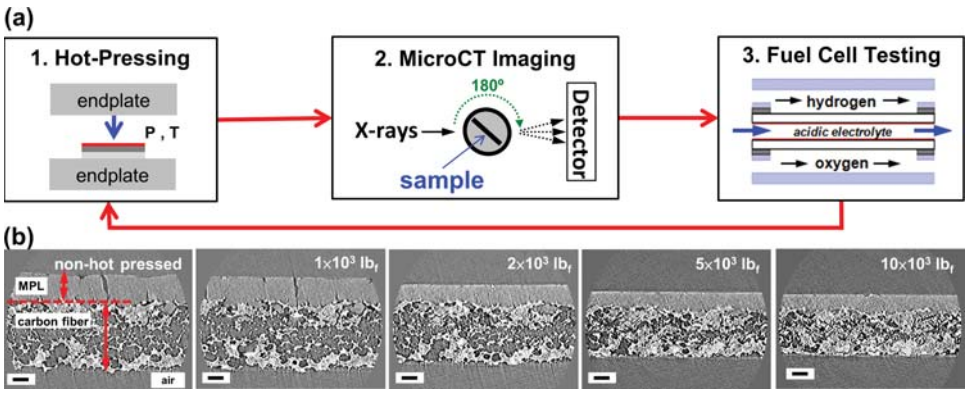

Figure 3. (a) Experimental protocol for investigating the relationship between electrode structure (via MicroCT imaging) and performance (via testing in an acidic fuel cell) as a function of hot-pressing the cathode at different pressures. (b) 2D through-plane radiographic images of the same cathode consecutively hot-pressed at different pressures.

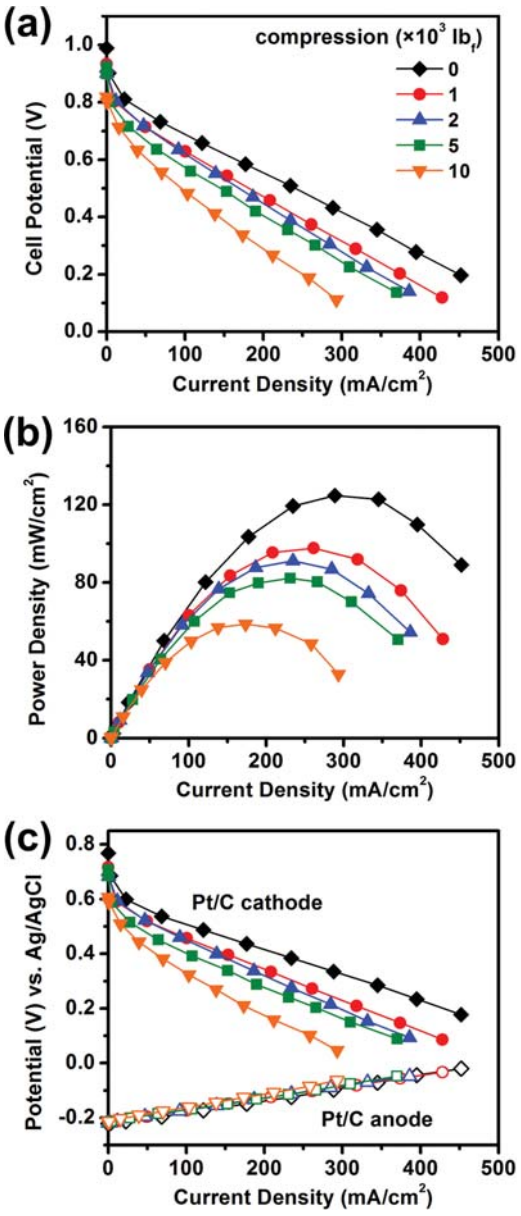

Figure 4. (a) Fuel cell polarization curve, (b) power density curve, and (c) corresponding individual electrode polarization curves, of the same cathode after hot-pressing at different pressures. Room temperature data; reactant streams: 10 sccm H_2/O_2; electrolyte: 1.0 M $HClO_4$ flowing at 0.6 mL/min.

sites and to effectively remove excess water from the porous electrode structure. One electrode is subjected repeatedly to a 3-step cycle (Figure 3a), namely hot-pressing (compression), microtomography (3D structural analysis), and microfluidic fuel cell testing (electrochemical performance). To start the process, a freshly-prepared electrode (0 lb_f) is analyzed in the MicroCT by securing the whole electrode in the rotating sample holder such that only a small marked corner was exposed to the X-ray beam between the source and detector. This enables multiple *ex-situ* analyzes of the same electrode volume after being exposed to different experimental conditions. After MicroCT analysis, the electrode is removed from the holder and used as a cathode in an acidic microfluidic H_2/O_2 fuel cell. Three polarization tests are performed, after which the cell is disassembled. The electrode is then hot-pressed at $P = 1 \times 10^3$ lb_f and $T = 125 \pm 10^{\circ}C$, followed by MicroCT analysis and electrochemical analysis. This cycle is repeated 3 more times, after applying increasing mechanical compressions (2×10^3, 5×10^3, and 10×10^3 lb_f, respectively). Whereas only one electrode was used to collect the specific dataset reported in Figures 3–6, we analyzed multiple electrodes in a similar way, which all provided similar results. Figure 3b shows a representative series of through-plane (XZ-plane) images *of the same electrode* as a function of mechanical compression force. While both the MPL and carbon fiber layer are compressed with increasing force, the majority of the compression is observed, as predicted, in the highly porous carbon fiber layer.

Figure 4 shows the effects of hot-pressing on the electrochemical performance of the cathode within the acidic fuel cell. The fuel cell polarization curve (Figure 4a) and power density curve (Figure 4b) as a function of hot-pressing pressure indicate that the overall fuel cell performance decreases with increasing compression. The corresponding individual electrode polarization curves show that these changes in overall fuel cell performance can be attributed to decreases in cathode performance (Figure 4c). As the cathode compresses, the onset potential decreases indicating reduced availability of catalytic sites, and ohmic losses increase indicating reduced reactant transport to the catalyst layer and, to a lesser extent, damaged carbon fiber connectivity in the macroporous layer (higher resistivity). As expected, the anode performance does not change, because the same, un-compressed anode was used for all experiments.

Next, we related electrochemical performance data to structural characteristics. Figure 5a correlates *bulk* porosity of the cathode carbon fiber layer, obtained via MicroCT imaging, and fuel cell performance (normalized peak power density). Prior to compression, the bulk porosity of the carbon fiber layer is $70.6 \pm 0.9\%$ which is in good agreement with previous reports.[38] The subsequent reductions in porosity of the carbon fiber layer of the cathode (as a result of hot pressing) follow the same trend as the observed decreases in fuel cell performance. Only when going from no compression to a compression of 1×10^3 lb_f, the drop in fuel cell peak power density appears to be more than the drop observed at higher pressures. At low compression, shifts in MPL and catalyst layer structures are likely responsible for a reduction in electrode performance, which we are presently studying in more detail. Figure 5b–5d show the correlation of fuel cell performance and bulk tortuosity, relative diffusivity, and permeability of the cathode carbon fiber layer, respectively, as a function of compression. As the compression increases, the reduction in porosity of the carbon fiber layer results in increases in tortuosity and in decreases in relative diffusivity as well as permeability.

Next we investigated the effects of hot-pressing on the *local* physical structure of the cathode (Figure 6). By segmenting the carbon fiber layer into 10 normalized regions in both the through-plane (Figure 6a) and in-plane (not shown) directions, the effects of compression on local porosity can be analyzed. Figure 6b shows the change in through-plane porosity distribution as a function of mechanical compression. The increase in porosity toward the center of the macroporous layer structure indicates that the carbon fiber layer was constructed by pressing two thinner carbon fiber layers via ply molding manufacturing.[39] The porosity drops at the edges due to the uneven distribution of PTFE throughout the sample including the formation of a PTFE "skin" on outer edges of the backing layer, as has been reported by Fluckiger et al.[33] as well as Fishman et al.[40] and independently observed here (Figure 1a2). Initially, when going from no compression to a compression pressure of 1×10^3 lb_f, the porosity distribution shifts and reduces slightly as the MPL compacts into the carbon fiber layer (Figure 6b). Between compressions of 1×10^3 and 5×10^3 lb_f, the porosity distribution remained constant (curves all have the same shape) while the bulk porosity reduces substantially (curves shift down). At compressions greater than 5×10^3 lb_f the porosity appears to approach a minimum value which is likely due to the formation of solid stacks of carbon fiber which cannot be compressed further easily, as observed in Figure 3b. While the porosity varies significantly in the through-plane directions, the in-plane porosity (both in the YZ- and XY-plane) varies only slightly (Figure 6c), with these slight variations probably due to in-plane anisotropy of the carbon paper. Interestingly,

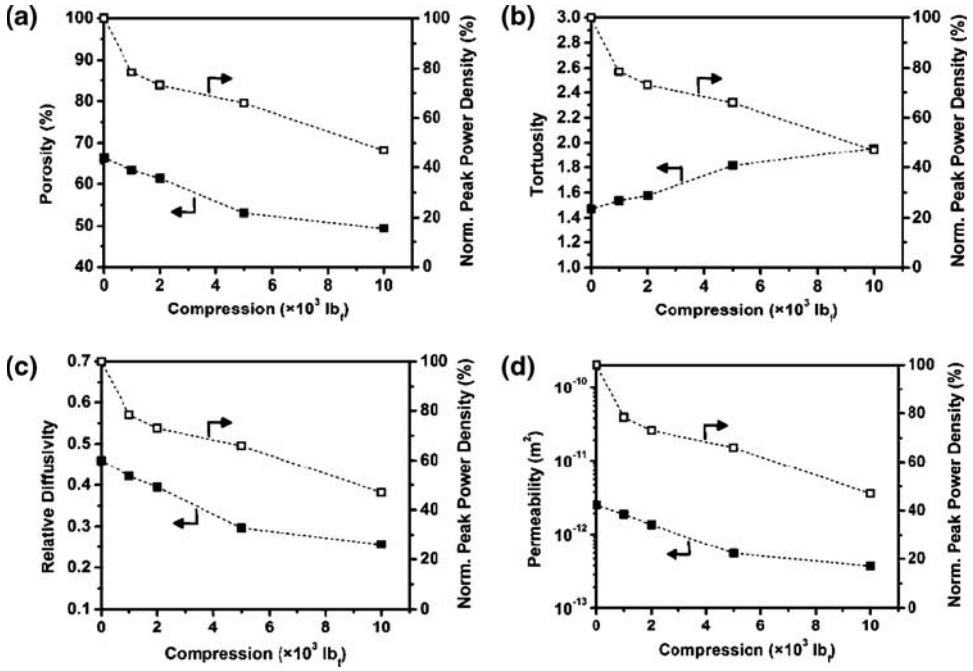

Figure 5. Normalized acidic fuel cell peak power density and related (a) bulk porosity, (b) bulk tortuosity, (c) bulk relative diffusivity, and (d) bulk permeability of the cathode as a function of compression.

both in- and through-plane porosity distributions remains constant independent of the amount of mechanical compression applied.

Based on the through-plane porosity distribution data shown in Figure 6b, the corresponding through-plane distribution of physical properties such as tortuosity (Figure 6d), relative diffusivity (Figure 6e), and permeability (Figure 6f) can be calculated as a function of cathode compression using equations 3, 4, and 6 respectively. In general, tortuosity decreases with an increase of porosity whereas relative diffusivity and permeability increase with an increase of porosity. The through-plane heterogeneity of these transport

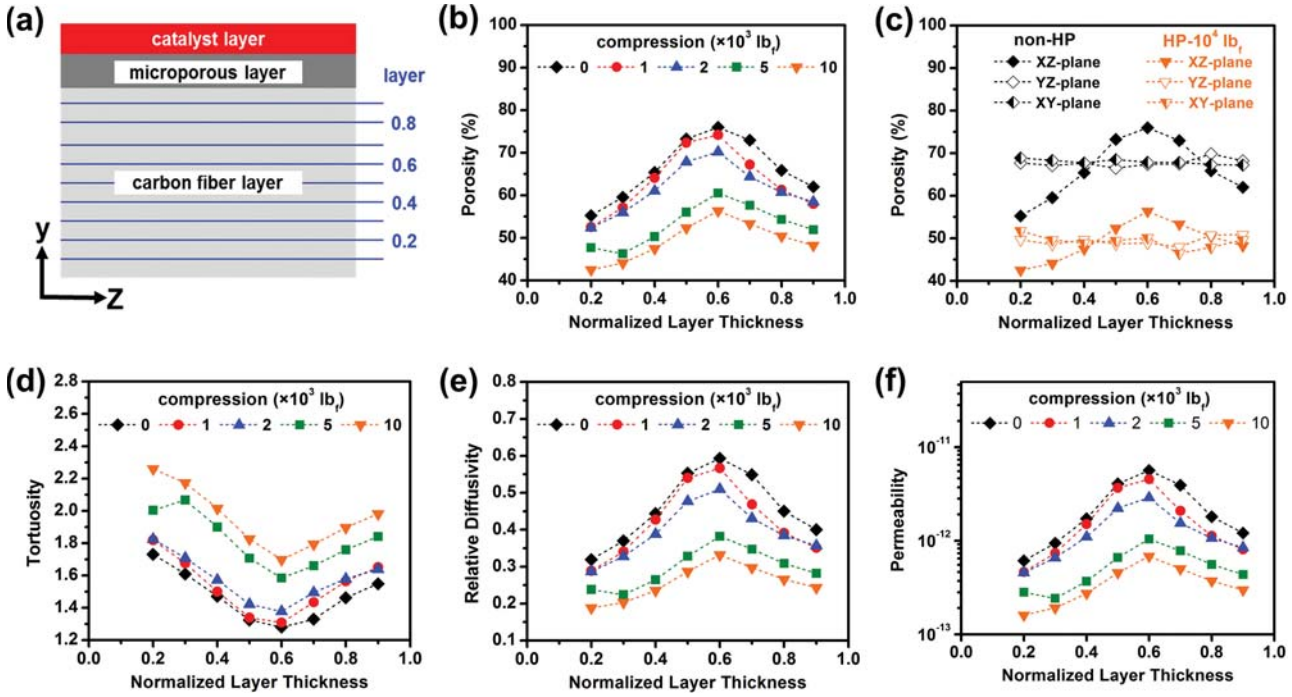

Figure 6. Local in-plane and through plane porosity distribution and related physical properties of the carbon fiber layer of a cathode hot-pressed at different pressures: (a) Segmentation of the carbon fiber layer into 10 normalized regions in the through-plane direction (XZ-plane, not drawn to scale). (b) Local through-plane porosity distribution as a function of cathode compression (YZ-plane). (c) Comparison of local porosity distribution of a non-hot pressed and hot-pressed (10^4 lb_f) cathode for all three possible planes. Local through-plane distribution of (d) tortuosity, (e) relative diffusivity, and (f) permeability as a function of cathode compression.

properties observed here is in good agreement with previous reports.[24] The heterogeneity of these physical properties, which significantly affect transport through the electrode, should be considered for future development of multiphase transport models, especially for numerical water management models since the heterogeneous pore structure of GDLs is likely to cause liquid water retention in certain regions within GDLs.[41]

In summary, the data reported above indicates that fuel cell electrode performance is very sensitive to changes in structure due to compression. In specific, both subtle shifts in structure in the MPL and catalyst layers at low compression pressures ($<1 \times 10^3$ lb_f) and more drastic structural densification of the macroporous carbon fiber layer at moderate compression pressures ($\geq 1 \times 10^3$ lb_f) affect electrode performance. Mechanical compression during electrode preparation and within the stack after assembly should be minimized to prevent permanent changes to the electrode structure to avoid loss in performance.

Conclusions

In this paper we demonstrated the utility of MicroCT for the detailed characterization of the 3D architecture of fuel cell electrodes, specifically the structure of the different layers and the interfaces between those layers, in a non-destructive fashion. Comprehensive information about layer thickness, internal architecture, and material distribution can be obtained from 2D radiographic cross-sectional image stacks and 3D tomographic virtual models of the GDE. The quality of these analyses depends on the thoroughness of the protocols used for post-image processing. Here we applied for the first time a filament tracing segmentation method to the characterization of fuel cell electrodes. This method utilizes structural connectivity in combination with grayscale thresholding, whereas existing methods use grayscale thresholding only. The use of structural connectivity information better differentiates fibrous masses within the electrode structure from void space, leading to a more accurate segmentation, and thus more accurate structural information.

Changes in electrochemical performance, as measured *in-situ* using a microfluidic H_2/O_2 fuel cell, can be correlated directly to changes in physical structure (i.e., porosity), as determined *ex-situ* using MicroCT. We observed that fuel cell electrode performance is very sensitive to changes in structure due to compression. Both subtle shifts in structure in the MPL and catalyst layers at low compression pressures ($<1 \times 10^3$ lb_f) and more drastic structural densification of the macroporous carbon fiber layer at moderate compression pressures ($\geq 1 \times 10^3$ lb_f) affect electrode performance. While hot-pressing is typically used in the assembly of fuel cell electrodes to enhance interlayer bonding, our study shows that mechanical compression during electrode preparation and within the stack after assembly should be minimized to prevent changes to the electrode structure that are detrimental to their electrochemical performance. For the GDL studied here, we concluded that a pressure less than 1×10^3 lb_f should be applied. However, this value is likely to be highly-dependent on the nature of the exact composition of the components (i.e., GDL type, membrane, catalyst layer) used. The MicroCT-based imaging and filament tracing post-processing methods presented here can also be used to probe for changes in the catalyst layer and the MPL (e.g., the effect of PTFE treatment) as a function of processing parameters. More generally, this study shows that systematic investigation of structure-activity relationships as enabled by the capabilities of MicroCT-analytical methods will benefit the rational design of novel highly active and durable electrodes, be it for fuel cells or for other energy conversion applications.

Acknowledgment

We gratefully acknowledge financial support from the Department of Energy (grant DE-FG02005ER46260) and the National Science Foundation (Career grant CTS 05-47617).

References

1. L. Carrette, K. A. Friedrich, and U. Stimming, *Fuel Cells*, **1**, 5 (2001).
2. J. M. R. Borup, B. Pivovar, Y. S. Kim, R. Mukundan, N. Garland, D. Myers, M. Wilson, F. Garzon, D. Wood, P. Zelenay, K. More, K. Stroh, T. Zawodzinski, J. Boncella, J. E. McGrath, M. Inaba, K. Miyatake, M. Hori, K. Ota, Z. Ogumi, S. Miyata, A. Nishikata, Z. Siroma, Y. Uchimoto, K. Yasuda, K. I. Kimijima, and N. Iwashita, *Chemical Reviews*, **107**, 3904 (2007).
3. M. Jacoby, *Chem. Eng. News*, **87**, 39 (2009).
4. L. Cindrella, A. M. Kannan, J. F. Lin, K. Saminathan, Y. Ho, C. W. Lin, and J. Wertz, *J Power Sources*, **194**, 146 (2009).
5. J. R. Wilson, W. Kobsiriphat, R. Mendoza, H. Y. Chen, J. M. Hiller, D. J. Miller, K. Thornton, P. W. Voorhees, S. B. Adler, and S. A. Barnett, *Nat Mater*, **5**, 541 (2006).
6. H. Ostadi, P. Rama, Y. Liu, R. Chen, X. X. Zhang, and K. Jiang, *J Membrane Sci*, **351**, 69 (2010).
7. S. Zils, M. Timpel, T. Arlt, A. Wolz, I. Manke, and C. Roth, *Fuel Cells*, **10**, 966 (2010).
8. S. R. Stock, *MicroComputed Tomography : methodology and applications*, p. 331, CRC Press, Boca Raton (2009).
9. S. R. Stock, *International Materials Reviews*, **53**, 129 (2008).
10. P. K. Sinha, P. Halleck, and C. Y. Wang, *Electrochem Solid St*, **9**, A344 (2006).
11. P. K. Sinha, P. P. Mukherjee, and C. Y. Wang, *J Mater Chem*, **17**, 3089 (2007).
12. A. Bazylak, *Int. J. Hydrog. Energy*, **34**, 3845 (2009).
13. F. N. Buchi, R. Fluckiger, D. Tehlar, F. Marone, and M. Stampanoni, *ECS Transactions*, **16**, 587 (2008).
14. P. Rama, Y. Liu, R. Chen, H. Ostadi, K. Jiang, X. X. Zhang, R. Fisher, and M. Jeschke, *J Fuel Cell Sci Tech*, **7** (2010).
15. J. Becker, R. Fluckiger, M. Reum, F. N. Buchi, F. Marone, and M. Stampanoni, *J Electrochem Soc*, **156**, B1175 (2009).
16. H. Ostadi, P. Rama, Y. Liu, R. Chen, X. Zhang, and K. Jiang, *Microelectron Eng*, **87**, 1640 (2010).
17. H. Ostadi, P. Rama, Y. Liu, R. Chen, X. X. Zhang, and K. Jiang, *Chem Eng Sci*, **65**, 2213 (2010).
18. J. Hinebaugh, Z. Fishman, and A. Bazylak, *J. Electrochem. Soc.*, **157**, B1651 (2010).
19. H. Ostadi, K. Jiang, and P. D. Prewett, *Micro Nano Lett*, **3**, 106 (2008).
20. Z. Fishman, J. Hinebaugh, and A. Bazylak, *J Electrochem Soc*, **157**, B1643 (2010).
21. N. S. K. Gunda, H. W. Choi, A. Berson, B. Kenney, K. Karan, J. G. Pharoah, and S. K. Mitra, *J Power Sources*, **196**, 3592 (2011).
22. F. R. Brushett, W. P. Zhou, R. S. Jayashree, and P. J. A. Kenis, *J Electrochem Soc*, **156**, B565 (2009).
23. R. S. Jayashree, M. Mitchell, D. Natarajan, L. J. Markoski, and P. J. A. Kenis, *Langmuir*, **23**, 6871 (2007).
24. Z. Fishman and A. Bazylak, *J Electrochem Soc*, **158**, B247 (2011).
25. K. N. Grew, Y. S. Chu, J. Yi, A. A. Peracchio, J. R. Izzo, Y. Hwu, F. De Carlo, and W. K. S. Chiu, *J Electrochem Soc*, **157**, B783 (2010).
26. C. Kirbas and F. Quek, *Acm Computing Surveys*, **36**, 81 (2004).
27. H. Zhang, J. E. Fritts, and S. A. Goldman, *Comput Vis Image Und*, **110**, 260 (2008).
28. I. H. Parkinson, A. Badiei, and N. L. Fazzalari, *Australas Phys Eng S*, **31**, 160 (2008).
29. D. A. G. Bruggeman, *Ann. phys.*, **24**, 636 (1935).
30. M. M. Tomadakis and S. V. Sotirchos, *Aiche J*, **37**, 74 (1991).
31. M. M. Tomadakis and S. V. Sotirchos, *Aiche J*, **39**, 397 (1993).
32. A. Z. Weber and J. Newman, *Chem. Rev.*, **104**, 4679 (2004).
33. R. Fluckiger, S. A. Freunberger, D. Kramer, A. Wokaun, G. G. Scherer, and F. N. Buchi, *Electrochim Acta*, **54**, 551 (2008).
34. J. T. Gostick, M. W. Fowler, M. D. Pritzker, M. A. Ioannidis, and L. M. Behra, *J Power Sources*, **162**, 228 (2006).
35. C. H. H. W. K. Lee, J. W. Van Zee, and M. Murthy, *Journal of Power Sources*, **84**, 45 (1999).
36. J. B. Ge, A. Higier, and H. T. Liu, *J Power Sources*, **159**, 922 (2006).
37. N. Djilali, A. Bazylak, D. Sinton, and Z. S. Liu, *Journal of Power Sources*, **163**, 784 (2007).
38. G. Y. Lin and T. Van Nguyen, *J Electrochem Soc*, **152**, A1942 (2005).
39. J. R. M. Mathias, J. Fleming, and W. L. Lehnert, *Handbook of Fuel Cells: Fundamentals, Technology, and Applications*, John Wiley & Sons, New York (2003).
40. Z. Fishman and A. Bazylak, *J Electrochem Soc*, **158**, B841 (2011).
41. R. Fluckiger, F. Marone, M. Stampanoni, A. Wokaun, and F. N. Buchi, *Electrochim Acta*, **56**, 2254 (2011).